Semiconducting Monolayer Materials as a Tunable Platform for Excitonic Solar Cells

Marco Bernardi,[†] Maurizia Palummo,[†,‡] and Jeffrey C. Grossman[†,*]

[†]Department of Materials Science and Engineering, Massachusetts Institute of Technology, 77 Massachusetts Avenue, Cambridge Massachusetts 02139-4307, United States and [‡]Dipartimento di Fisica, Università di Roma Tor Vergata, CNISM, and European Theoretical Spectroscopy Facility (ETSF), Via della Ricerca Scientifica 1, 00133 Roma, Italy

ABSTRACT The recent advent of two-dimensional monolayer materials with tunable optical properties and high carrier mobility offers renewed opportunities for efficient, ultrathin excitonic solar cells alternative to those based on conjugated polymer and small molecule donors. Using first-principles density functional theory and many-body calculations, we demonstrate that monolayers of hexagonal BN and graphene (CBN) combined with commonly used acceptors such as PCBM fullerene or semiconducting carbon nanotubes can provide excitonic solar cells with tunable absorber gap, donor–acceptor interface band alignment, and power conversion efficiency, as well as novel device architectures. For the case of CBN–PCBM devices, we predict power conversion efficiency limits in the 10–20% range depending on the CBN monolayer structure. Our results demonstrate the possibility of using monolayer materials in tunable, efficient, ultrathin solar cells in which unexplored exciton and carrier transport regimes are at play.

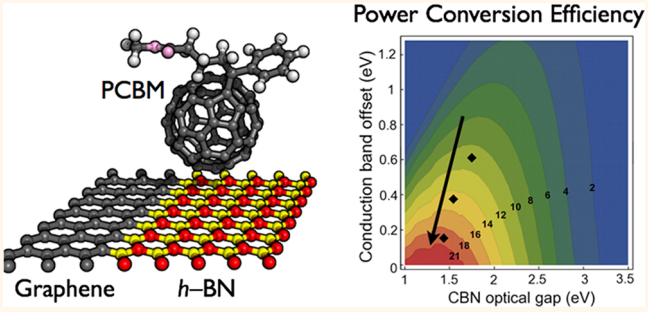

KEYWORDS: photovoltaics · graphene · boron nitride · monolayer materials · band offsets · power conversion efficiency

Solar cell devices converting energy radiated from the sun to electricity have developed into two main families: those based on bulk inorganic semiconductors such as Si, GaAs, CdTe, and CIGS,[1] in which free charge carrier generation follows light absorption without intermediate steps, and those based on conjugated polymers and small molecules[2,3] or other materials where following light absorption a complex of hole and electron carriers (exciton) is formed with a binding energy in large excess of *kT*. The latter type, referred to as excitonic solar cell (XSC),[4] realizes charge carrier generation by dissociating bound excitons at semiconductor heterointerfaces, owing to discontinuities across the interface in the electron affinity and ionization potential.

A typical solid state XSC[5] employs a donor–acceptor blend of conjugated polymer or small molecule donors with high optical absorption in the visible, and fullerene derivative acceptors (*e.g.*, C_{60}, PCBM or similar fullerene molecules).[2,6,7] In such devices, the polymer donor dominates (and limits) the key physical processes in the solar cell, including optical absorption and transport of excitons and charge carriers. In particular, exciton diffusion lengths of 5–10 nm prevent the use of bilayer devices, and mobilities lower than 1 $cm^2/(V\,s)$ limit the thickness of bulk heterojunction devices to less than the absorption depth (typically 0.1–1 μm), thus limiting the output current.

In addition, tuning the highest occupied molecular orbital (HOMO) and lowest unoccupied molecular orbital (LUMO) levels of conjugated polymers is a challenging task, requiring trial and error chemical synthesis of a large number of compounds; band gaps of less than 1.5 eV are hard to achieve, and thus the absorption loss in the red part of the solar spectrum can be significant.[3] Despite such inherent material limitations and the related constraints they place on the device architecture, polymer and small molecule XSC technologies have progressed to impressive power conversion efficiencies of up to ~11%.[8,9]

* Address correspondence to jcg@mit.edu.

Received for review August 21, 2012 and accepted October 12, 2012.

Published online October 13, 2012
10.1021/nn303815z

Alternative XSC technologies have emerged in recent years, including efficient quantum-dot-based[10] and more recently nanocarbon-based XSC.[11] The key advantage of these novel excitonic devices is the possibility of altering the HOMO and LUMO levels, the band alignment, and the optical absorption using quantum confinement in nanomaterials in addition to just different chemistries as in the case of polymers and small molecules. Of great relevance is also the possibility of realizing novel device architectures,[10] while retaining the inherent advantages of solution processability and low temperature manufacturing typical of XSC.

In this context, the recent advent of two-dimensional (2D) monolayer materials with tunable optical properties and high carrier mobility, such as monolayers of graphene,[12] graphene-BN,[13−15] MoS_2,[16,17] and other transition-metal oxides and dichalcogenides,[18] offers renewed opportunities for thin-film XSC. Several such 2D monolayer materials present very strong optical absorption at photon energies of interest in photovoltaics. For example, one layer of graphene can absorb 2.3% of incident photons at visible wavelengths[19] within a van der Waals stacking thickness of only 3.3 Å in the direction normal to the layer, while MoS_2 and $MoSe_2$ monolayers present optical gaps in the range of 1.5−2 eV.[16,18] By stacking multiple layers of graphene or other 2D materials with a total thickness as small as 50−100 nm, a significant fraction of incoming sunlight could be captured.

Although graphene is a semimetal that can only be used in Schottky-type solar cells,[20] other monolayers are semiconductors with strong excitonic effects and could be combined to form efficient XSC. Possible strategies for tuning the optical and electronic properties of monolayer materials include the formation of domains with quantum confinement within the layer,[15] or the use of stackings of different monolayers to create novel van der Waals structures.[21] An example of the former strategy is the case of hybridized graphene-BN (CBN) monolayers,[13−15] whose electronic band gap, optical absorption, and exciton binding energy can be varied by tuning the C domain size and shape, due to quantum confinement of carriers and excitons within the C domains.[15] As a further point of novelty, carrier and exciton transport in solar cells based on 2D monolayers could occur in a different regime than in conventional photovoltaic materials, due to the peculiar nature of electron−phonon coupling in monolayer materials.[22−24] Operation regimes including hot carrier extraction and coherent exciton transport could be envisioned and tested using ultrathin solar cells based on a few monolayers.

In this work, we employ *ab initio* calculations to study interfaces between CBN monolayers and carbon-based acceptors such as PCBM and semiconducting single-walled carbon nanotubes (s-SWCNT).

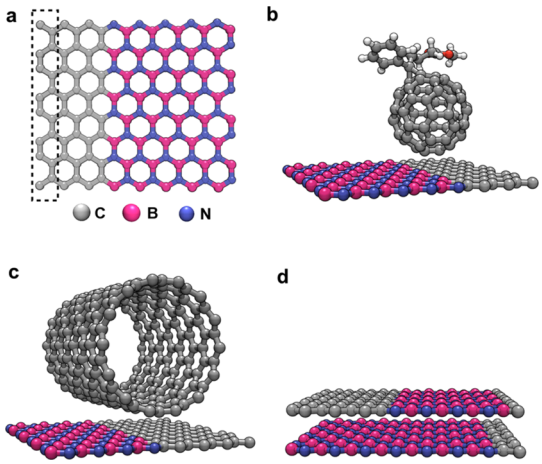

Figure 1. (a) CBN monolayer unit cell used in our DFT calculations, with an armchair edge between the C and BN domains. Shown in the dashed box is a C atom row, with an approximate width of 0.25 nm. Following the nomenclature used here, the unit cell shown is $C_3(BN)_5$. Panels b−d show interfaces between a CBN monolayer and (b) PCBM fullerene, (c) a (14,0) zigzag SWCNT, and (d) another CBN layer with different composition.

We demonstrate that such CBN monolayer interfaces can form tunable type-II band alignment,[25] and hold promise to realize exciton dissociation in 2D monolayer based solar cells. We show that the photovoltaic power conversion efficiency resulting from such CBN interfaces can be significantly tuned by varying the carbon domain size in the CBN monolayer, with predicted upper efficiency limits in the 10−20% range. Our calculations further suggest that even just two stacked monolayers of CBN with the proper structure could constitute an ultrathin solar cell with ∼3 Å thickness, thus allowing one to investigate carrier and exciton transport at very short time and length scales during photovoltaic operation.

RESULTS AND DISCUSSION

***Ab Initio* Calculations and CBN Interfaces.** We study model CBN systems constituted by a monolayer with C and BN stripe domains arranged in a 2D superlattice and separated by an armchair edge. The CBN repeat unit consists of a layer with eight atom rows and an overall composition of $C_x(BN)_{(8-x)}$, where x is the number of C rows in the structure, each 0.25 nm wide (Figure 1a).[26]

Interfaces containing CBN sheets (Figure 1b−d) are formed by placing PCBM, or s-SWCNT of chirality (10,0), (14,0), and (16,0), or a second CBN layer at a van der Waals distance of 3.3 Å from a given CBN monolayer. In CBN bilayer calculations, the unit cell consists of two $C_x(BN)_{(8-x)}$ layers with AB stacking in the BN domains (B atoms on top of N atoms).[27] We compute the electronic structure of such CBN interfaces by means of *ab initio* density functional theory (DFT) calculations with a plane-wave basis set, using the QUANTUM ESPRESSO code[28] (see Methods).

The DFT band offsets are estimated in all cases as differences in the peaks of the projected density of

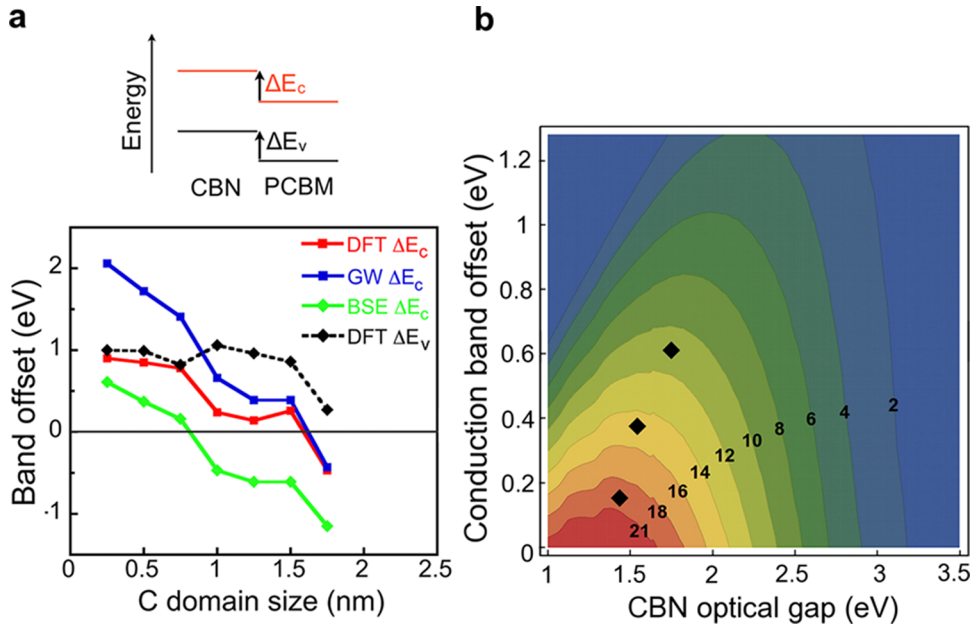

Figure 2. (a) DFT valence band offset (ΔE_v, dashed curve) and DFT, GW, and BSE conduction band offsets (ΔE_c, solid curves) between $C_x(BN)_{(8-x)}$ monolayers and PCBM fullerene, expressed as a function of the C domain size in the CBN layer. ΔE_v and ΔE_c are referenced, respectively, to the valence and conduction band edges of the acceptor, as shown schematically above the plot. Within our model, ΔE_v is the same at all levels of theory since the GW corrections were applied as a rigid shift of the LUMO levels (see Methods). The number *x* of C atom rows in the CBN superlattice structure increases by one unit (from 1 to 7) at each consecutive point in the plot, and for each added row the C lateral domain size increases by 0.25 nm. The alignment is consistently found to be type-II for C domain sizes of up to approximately 1−2 nm depending on the level of theory used. (b) Power conversion efficiency contour plot as a function of the CBN donor optical gap and conduction band offset ΔE_c. Constant efficiency level curves up to 21% are shown in the figure. The diamonds represent the efficiency limits of the three CBN−PCBM combinations yielding type-II alignment in the BSE curve in panel a. Efficiency values in the 10−20% range are predicted depending on the C domain size.

states (PDOS) for the two structures constituting the interface.[29] While this approach is usually reliable for the estimate of valence band offsets,[30] the accuracy of conduction band offsets depends on a compensation of errors on the DFT band gap of the two materials constituting the interface. Hence for the case of CBN−PCBM interfaces, we choose to compute band offsets with higher accuracy at the GW and GW plus Bethe−Salpeter equation (GW + BSE) levels of theory (see Methods), justified by our interest in computing the power conversion efficiency of CBN−PCBM interfaces, a quantity rather sensitive to errors in the optical gaps and interface band offsets. On the other hand, for the CBN−SWCNT and CBN bilayer interfaces our analysis is based solely on DFT results, and is mainly aimed at determining qualitatively the possibility of forming type-II interfaces involving CBN monolayers.

Band Offsets and Efficiency in CBN−PCBM Interfaces. Figure 2a shows DFT valence band offsets (ΔE_v) and conduction band offsets (ΔE_c) at different levels of theory for interfaces between PCBM and $C_x(BN)_{(8-x)}$ monolayers with different C domain sizes. Each consecutive point represents the addition of one C atom row and the removal of one BN row in the unit cell (Figure 1a), leading to a 0.25 nm increase of the C domain size. The DFT band alignment is found to be type-II for C domain sizes of up to 1.5 nm, with the PCBM acting as the acceptor at the interface, as seen by the positive values of ΔE_v and ΔE_c using the convention shown in Figure 2a. The trends in ΔE_v and ΔE_c show that the HOMO and LUMO energies of the donor can be tuned according to the C domain size, yielding a unique control over the interface band offsets. This results in a tunable power conversion efficiency, as explained below.

To confirm the type-II alignment found within DFT, we apply GW corrections separately to the LUMO levels of CBN and PCBM (see Methods and Supporting Material). The GW corrected ΔE_c values,[31] shown in Figure 2a (GW curve) yield the same qualitative trends as the DFT results, with type-II alignment for C domain sizes of up to 1.5 nm.

Assuming that CBN is the main absorber in the solar cell, the exciton binding energy in the CBN layer is a key quantity to determine the energetics of photoexcited electron transfer to PCBM. To address this point, we calculate ΔE_c values as differences between the optical LUMO level of the CBN donor (using GW + BSE, and thus accounting for exciton binding energy) and the GW LUMO level of the PCBM acceptor. This *combined scheme* utilizing the optical LUMO of the donor and the quasiparticle LUMO of the acceptor takes into account the minimum energy of the exciton formed after photoabsorption in the CBN donor, as well as the

electronic quasiparticle level for the transfer of a photoexcited electron to the acceptor. The ΔE_c values derived at this combined level of theory are shown in Figure 2a (BSE ΔE_c curve), and are used below to compute power conversion efficiencies; within this approximation, the useful range for XSC operation is restricted to C domain sizes of up to ~1 nm, for which the $\Delta E_c > 0$ condition is met.[32]

The three CBN–PCBM interfaces satisfying this condition include the CBN layers $C_1(BN)_7$, $C_2(BN)_6$, and $C_3(BN)_5$, as seen from the BSE curve in Figure 2a. For these cases, we estimate here a practical upper limit to the power conversion efficiency.

Though the thermodynamic efficiency limit for thermalized carriers and in the absence of nonradiative recombination is set by the optical gap of the donor through the Schockley–Quisser limit,[4,33] *trends and practical efficiency limits* are far more useful for XSC than ultimate thermodynamic limits.[34,35]

Following Scharber *et al.*,[34] we estimate maximum power conversion efficiencies η for CBN–PCBM devices with type-II alignment as

$$\eta = \frac{0.65(E_g^{\mathrm{opt,d}} - \Delta E_c - 0.3)\int_{E_g^{\mathrm{opt,d}}}^{\infty} \frac{J_{\mathrm{ph}}(\hbar\omega)}{\hbar\omega}\,\mathrm{d}(\hbar\omega)}{\int_{E_g^{\mathrm{opt,d}}}^{\infty} J_{\mathrm{ph}}(\hbar\omega)\,\mathrm{d}(\hbar\omega)} \quad (1)$$

where 0.65 is the fill factor (FF), J_{ph} ($\hbar\omega$) is the AM1.5 solar energy flux (expressed in W m^{-2} eV^{-1})[36] at the photon energy $\hbar\omega$, and $E_g^{\mathrm{opt,d}}$ is the optical band gap of the CBN donor.

In eq 1, the $(E_g^{\mathrm{opt,d}} - \Delta E_c - 0.3)$ term is an estimate of the maximum open circuit voltage (V_{oc}, here in eV units), calculated as the effective interface gap ($E_g^{\mathrm{opt,d}} - \Delta E_c$) taken here between the DFT HOMO level of the donor and the GW LUMO level of the acceptor, minus 0.3 eV, which accounts for energy conversion kinetics.[34,37] The integral in the numerator is the short circuit current J_{sc} calculated using a limit external quantum efficiency (EQE) of 100%, while the denominator is the integrated AM1.5 solar energy flux, which amounts to 1000 W/m^2. The efficiency η is thus estimated as the product $FF \cdot V_{oc} \cdot J_{sc}$ normalized by the incident energy flux, in the limit of 100% EQE.[38]

Figure 2b shows the efficiency of the three CBN–PCBM interfaces with type-II alignment, as a function of the CBN donor optical gap and the interface ΔE_c, the latter computed as the difference between the optical LUMO level of CBN and the GW LUMO level of PCBM, as explained above. For the $C_1(BN)_7$, $C_2(BN)_6$, and $C_3(BN)_5$ monolayers, the computed efficiency values are, respectively, 11%, 15%, and 20%. Assuming an error $\Delta E_g^{\mathrm{opt,d}}$ of ~0.1 eV in the calculation of the optical gap, and an error ΔV_{oc} on the interface electronic gap (and thus on V_{oc}) also of 0.1 eV, the relative error on the efficiency $\Delta\eta/\eta$ can be calculated as

$$\frac{\Delta\eta}{\eta}(\Delta E_g^{\mathrm{opt,d}}, \Delta V_{oc}) = \frac{1}{\eta}\sqrt{\left[\left(\frac{\partial\eta}{\partial V_{oc}}\right)\Delta V_{oc}\right]^2 + \left[\left(\frac{\partial\eta}{\partial E_g^{\mathrm{opt,d}}}\right)\Delta E_g^{\mathrm{opt,d}}\right]^2}$$

Using $\Delta E_g^{\mathrm{opt,d}} = \Delta V_{oc} = 0.1$ eV, and the optical gaps and V_{oc} values found here, the relative errors for the three cases shown in Figure 2b are estimated to be of the order of $\Delta\eta/\eta \approx 0.1$–$0.15$. This translates to an overall efficiency range of $\eta = 11$–$20 \pm 3\%$ for the three cases studied here.

The striking efficiency tunability found here is achieved by changing the C domain size within the CBN monolayer over a 1 nm range. Though such small C domains might seem challenging to achieve in practice, the immiscibility of C and BN in a monolayer leads to the formation of a large amount of subnanometer scale domains, to the point that single C and BN domains cannot be resolved in as-synthesized CBN monolayers.[13] While several approaches for controlling the domain size and shape at the atomistic scale in CBN are being actively explored,[14,39] the strategy found here of lateral quantum confinement in 2D monolayers to achieve tunability in XSC is general and can be extended to other monolayer materials.

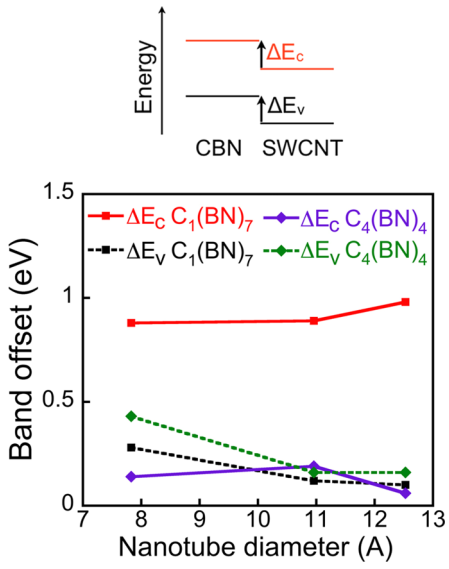

Figure 3. Valence (ΔE_v) and conduction (ΔE_c) band offsets at CBN–SWCNT interfaces, calculated using DFT and shown here for combinations of the two CBN structures $C_1(BN)_7$ and $C_4(BN)_4$ and the three zigzag nanotubes (10,0), (14,0), and (16,0). ΔE_v and ΔE_c are referenced, respectively, to the valence and conduction band edges of the acceptor, as shown above the plot, and are plotted as a function of nanotube diameter. Both ΔE_v (dashed lines) and ΔE_c (solid lines) are positive in all cases, indicating type-II alignment.

CBN–SWCNT and CBN Bilayer Interfaces. Next, we analyze the band alignment at CBN–SWCNT and CBN bilayer interfaces. While accurate band offset calculations were necessary to extract efficiency trends of CBN–PCBM interfaces, for the CBN–SWCNT and CBN bilayer systems our analysis is based on DFT without

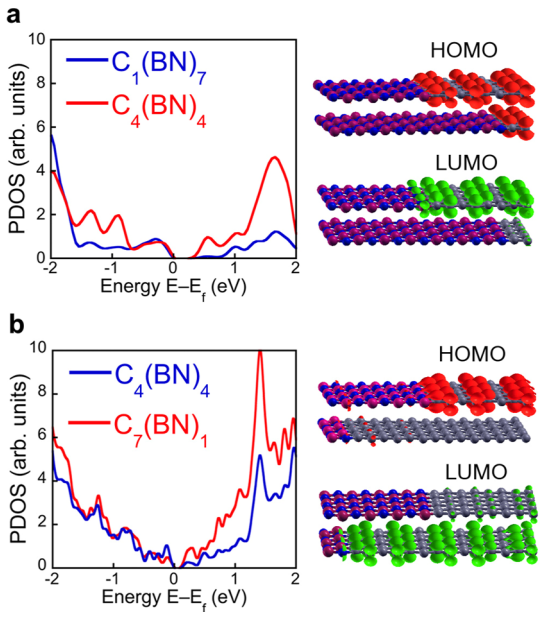

Figure 4. PDOS (left) and HOMO and LUMO orbital isosurfaces (right) for CBN bilayers studied using DFT. The energies in the PDOS plots are referenced to the Fermi energy E_f. Two monolayer combinations are shown: (a) $C_1(BN)_7$/$C_4(BN)_4$ and (b) $C_4(BN)_4$/$C_7(BN)_1$. Type-I or type-II band alignments are predicted depending on the structure and C domain size of the CBN layers composing the bilayer. The high-frequency oscillations seen in the PDOS curve in panel b near the band gap are an artifact due to Brillouin zone sampling in the DFT calculation.

further corrections, and has the main goal of qualitatively showing the possibility of forming type-II alignment at interfaces involving monolayer CBN. Figure 3 shows the DFT valence and conduction band offsets for interfaces between the two CBN systems $C_1(BN)_7$ and $C_4(BN)_4$ (with respectively 0.25 and 1 nm C domain size) and zigzag s-SWCNT with three different diameters. Both ΔE_v and ΔE_c are found to be positive (with the convention shown in Figure 3) for both CBN cases and regardless of the nanotube diameter, implying a type-II alignment for these interfaces. The band offsets show little variation with nanotube diameter, and ΔE_c becomes smaller for increasing C domain sizes, similar to the CBN–PCBM case. At the interface, the nanotube behaves as the acceptor, and should thus be n-doped in a real device for optimal performance. Similar to the case of CBN–PCBM interfaces, band offset values with a strong dependence on the C domain size in CBN are found, which could allow one to tune the solar cell performance by varying the structure of the CBN layer.

Though we do not verify it explicitly, the type-II alignment would be retained at the GW and GW + BSE levels of theory. For the alignment type to be inverted, the GW corrections to the nanotube band gap would need to be higher than the corresponding corrections to the CBN layer band gap, which are, respectively, 3.25 and 1.72 eV for the $C_1(BN)_7$ and $C_4(BN)_4$ cases.[15] However, only small GW corrections are predicted for

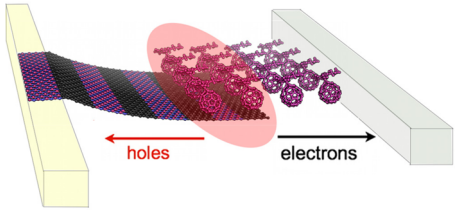

Figure 5. Proof-of-concept design of a solar cell based on 2D semiconducting monolayer materials, for the CBN–PCBM material combination. Note that the PCBM could be replaced by a second 2D monolayer, and the same architecture can be extended to other monolayer materials. The shaded oval indicates the interface where excitons are separated upon illumination (from the top in figure), and the arrows indicate the direction of carrier diffusion and extraction at the contacts, shown as thin metal fingers.

s-SWCNT in this diameter range (~10% of the band gap),[40] and such corrections certainly cannot be as large as 1.7 eV. Similar considerations hold for the GW + BSE level of theory, since the optical gaps of the two materials composing the interface are numerically close to the DFT gaps due to compensation of errors.[15]

As a last case study, we analyze the electronic structure and the PDOS of CBN bilayer systems, in which the two composing CBN monolayers have a different atomic structure and C domain size. Figure 4 shows the PDOS and the HOMO and LUMO orbitals of two bilayer cases among those studied in this work, calculated using DFT with a van der Waals corrected exchange-correlation functional (see Methods). In both bilayer systems, the LUMO localizes within the layer with the smaller energy gap. For the $C_1(BN)_7$/$C_4(BN)_4$ bilayer (Figure 4a), we observe a complete hybridization of the valence states, as seen by the perfect overlap of the valence PDOS, causing the HOMO to delocalize to both layers. In contrast, in the $C_4(BN)_4$/$C_7(BN)_1$ bilayer the HOMO is found to be localized on the $C_4(BN)_4$ layer, that is, the layer with the larger band gap. In this case, the incomplete hybridization of the valence states is seen by the slight valence band offset in the PDOS. We found an analogous behavior in the $C_1(BN)_7$/$C_7(BN)_1$ system.

On this basis, we predict the $C_1(BN)_7$/$C_4(BN)_4$ interface to be a type-I heterojunction with ohmic character (due to the absence of barriers for the transport of holes), and the $C_4(BN)_4$/$C_7(BN)_1$ and $C_1(BN)_7$/$C_7(BN)_1$ interfaces to be type-II heterojunctions, whereby exciton dissociation may be possible within a ~3.3 Å thick CBN bilayer. In both cases, the orbitals are predicted to dramatically change their spatial distribution upon photoexcitation (Figure 4), which may lead to opportunities for engineering the flow of photoabsorbed energy at the nanometer scale. We note that the alignment types found here for the bilayer systems would also be retained beyond the DFT level of theory, since the GW and the GW+BSE corrections to the band gaps are higher for the CBN monolayer with the larger band gap.[15]

Practical Implementation. Our results suggest that in principle it may be possible to fabricate a two atomic layer thick (~3.3 Å) XSC device by stacking two CBN monolayers with the proper C domain structures. Alternatively, given the tunability of the CBN layer electronic structure, a Schottky junction solar cell may be formed between a monolayer of graphene and a monolayer of CBN. While such a device would likely not absorb a significant fraction of sunlight, it could constitute a new platform for the experimental study of quantum transport effects (characteristic of 2D monolayers) under photovoltaic operation. For example, while hot carrier injection and hot exciton dissociation are possible at or near an interface,[41] in typical XSC such processes are hindered by diffusive transport through the bulk of the absorber. However, if a solar cell is made with a single monolayer or bilayer, no bulk diffusion would be involved and the hot carrier regime could be enabled. Similarly, it could be possible to study the impact of coherent exciton transport on XSC performance, a topic poorly explored in photovoltaics due to the fact that exciton transport operates in an incoherent regime in micrometer-thick bulk heterojunction solar cells.

As a test bed for these fundamental effects, we propose in Figure 5 an architecture whereby XSC based on 2D monolayer materials could be fabricated and characterized—for example using ultrafast spectroscopy measurements[42]—to study the presence of hot exciton or hot carrier effects.

In addition to opportunities for fundamental transport studies, ultrathin-monolayer-based XSC could be fabricated by stacking as few as ~50 monolayers with a total thickness of ~50 to 100 nm, a configuration that could suffice to absorb a significant fraction of incident sunlight with energy above the band gap.

Finally, we remark that while the tunability of the solar cell properties presented here originates from changes to the composition and domain structure of a single monolayer, additional tuning of physical quantities of interest in photovoltaics could be achieved by stacking sequences of different 2D semiconducting monolayers or by chemically functionalizing 2D monolayers, two approaches we are currently investigating.

CONCLUSION

We present the idea of XSC based on semiconducting 2D monolayer materials with the potential to achieve tunable 10−20% power conversion efficiencies, and show that combinations of CBN monolayers and PCBM or s-SWCNT are well-suited for the practical implementation of such devices. Even a photovoltaic device as thin as two atomic layers of CBN (or other monolayer materials with type-II band alignment) holds the potential to achieve solar energy conversion at exceptionally small length and ultrafast time scales. While a similar device configuration would allow one to probe transport in this poorly explored physical regime, multilayer stackings could be employed to absorb a significant fraction of incident sunlight, and could enable ultrathin (50−100 nm thick) solar cells based on photostable materials with high carrier mobility. The unique tunability in 2D monolayer materials of the band gap, interface band alignment, exciton binding energy, optical absorption, carrier mobility, and electron−phonon coupling entails new opportunities for fundamental studies and practical implementation of solar cell devices.

METHODS

Density Functional Theory Calculations. For all CBN interfaces studied here, an orthorhombic simulation cell was adopted, and all structures were fully relaxed within DFT to less than 30 meV/Å in the residual atomic forces. A 15 Å vacuum is placed in the direction normal to the CBN sheet to avoid spurious interactions with the image system. The Perdew−Burke−Ernzerhof exchange-correlation functional[43] is adopted, and ultrasoft pseudopotentials[44] are used to describe the core electrons. A kinetic energy cutoff of 35 Ry was used for the wavefunction and of 200 Ry for the charge density, in combination with converged Monkhorst-Pack $\vec{k}$-point grids[45] of up to 48 × 24 × 1. For the CBN bilayer calculations, the vdW-DF exchange-correlation functional[46] (as implemented in the QUANTUM ESPRESSO code) was employed to describe interlayer van der Waals interactions, both for structural relaxations and for band offset calculations.

GW and Bethe−Salpeter Calculations. To estimate the conduction band offsets with higher accuracy for the CBN−PCBM interfaces, we applied GW corrections[30] separately to the band gaps of the CBN and PCBM materials. For the three CBN monolayers $C_1(BN)_7$, $C_4(BN)_4$, and $C_7(BN)_1$, both the GW corrections and the GW + BSE optical gaps were taken from our previous work (see ref 15 for further details). As discussed in ref 15, six valence and eight conduction bands were used in the BSE, which were enough to achieve convergence in the optical BSE peaks up to approximately 6 eV. Consistent with previous work on 2D monolayers, the perturbative GW approach was used, and thus the states entering the BSE excitonic Hamiltonian are Kohn−Sham states. The corrections decrease linearly for increasing C domain size, so that corrections at intermediate C domain sizes were derived by interpolation (see Supporting Material). The GW correction for the PCBM electronic gap was calculated here using the Yambo code.[47] Briefly, we used the LDA exchange correlation functional[48] in combination with norm-conserving pseudopotentials[49] for the DFT ground-state calculation. The PCBM was studied in the solid state, using an orthorhombic unit cell containing one PCBM molecule, and choosing a 35 Ry kinetic energy cutoff and a 2 × 2 x 2 $\vec{k}$-point grid. The geometry was relaxed using both the LDA[48] and the vdW-DF[46] exchange correlation functionals, with analogous results. The cell size employed in the GW calculation was chosen as the one minimizing the total energy within LDA, which resulted in a density within 1% of the experimental value.[50] We employed a G_0W_0 update scheme in combination with a plasmon pole model for the dielectric function. Cutoffs of 35 and 8 Ry were used, respectively, for the exchange and correlation part of the self-energy, together with up to 1500 empty bands. We obtained an LDA gap of 0.9 eV, which summed to a GW correction of 1.2 eV yields an electronic quasiparticle gap of 2.1 eV, in excellent agreement with the experimental value

measured by photoemission techniques on a thin film of PCBM.[50] We remark that the GW correction needs to be applied to a condensed (rather than gas) PCBM phase in our systems in order to model the presence of the CBN at the interface, acting similarly to a continuous polarizable medium both in the CBN−PCBM interfaces used in the DFT calculations (whose band alignment we mean to correct), and in real interfaces within a thin film solar cell.

We note that if the GW correction was applied to the gas rather than condensed PCBM phase, a significantly larger GW correction would be found.[51] This effect is due to the difference in the ionization potential between the gas and condensed phases, and it derives from the polarization energy stabilizing the ionized molecule in the condensed phase.[50,52,53] For both the CBN and PCBM materials, the GW band gap corrections were converged to within 0.1 eV and the corrections to the single states to within 0.15−0.2 eV. In all cases studied here, the GW band gap correction is constituted for approximately 95% of the total by a shift of the LUMO level. For this reason, the entire value of the GW correction was applied in each case as a shift of the LUMO level (*i.e.*, we used a scissor operator approach), and thus the valence band offsets remain the same at all levels of theory in Figure 2a.

Conflict of Interest: The authors declare no competing financial interest.

Acknowledgment. M.B. acknowledges funding from Intel through the Intel Ph.D. Fellowship. We thank NERSC and Teragrid for providing computational resources.

Supporting Information Available: Fits of GW and BSE corrections applied to CBN. This material is available free of charge *via* the Internet at http://pubs.acs.org.

REFERENCES AND NOTES

1. Ginley, D.; Green, M. A.; Collins, R. Solar Energy Conversion Toward 1 Terawatt. *MRS Bull.* **2008**, *33*, 355–364.
2. Mayer, A. C.; Scully, S. R.; Hardin, B. E.; Rowell, M. W.; McGehee, M. D. Polymer-Based Solar Cells. *Mater. Today* **2007**, *10*, 28–33.
3. Nelson, J. Polymer:Fullerene Bulk Heterojunction Solar Cells. *Mater. Today* **2011**, *14*, 462–470.
4. Gregg, B. A. The Photoconversion Mechanism of Excitonic Solar Cells. *MRS Bull.* **2005**, *30*, 20–22.
5. Our discussion here does not include dye-sensitized solar cells, in which due to the presence of a liquid phase the carrier and exciton dynamics are different than in the solid state. Efficient solid-state dye-sensitized solar cells have also been shown recently, but they are not included in the present discussion.
6. Wienk, M. M.; Kroon, J. M.; Verhees, W. J. H.; Knol, J.; Hummelen, J. C.; van Hal, P. A.; Janssen, R. A. J. Efficient Methano[70]Fullerene/MDMO-PPV Bulk Heterojunction Photovoltaic Cells. *Angew. Chem., Int. Ed.* **2003**, *115*, 3493–3497.
7. Faist, M. A.; Keivanidis, P. E.; Foster, S.; Wobkenberg, P. H.; Anthopoulos, T. D.; Bradley, D. D. C.; Durrant, J.; Nelson, J. Effect of Multiple Adduct Fullerenes on Charge Generation and Transport in Photovoltaic Blends with Poly(3-hexylthiophene-2,5-diyl). *J. Polym. Sci, Part B: Polym. Phys* **2011**, *49*, 45–51.
8. The current efficiency record for small molecule based solar cells is 10.7% from the company Heliatex (see heliatex.com).
9. Dou, L.; You, J.; Yang, J.; Chen, C.-C.; He, Y.; Murase, S.; Moriarty, T.; Emery, K.; Li, G.; Yang, Y. Tandem Polymer Solar Cells Featuring a Spectrally Matched Low-Bandgap Polymer. *Nat. Photon.* **2012**, *6*, 180–185 After reporting 8.6% efficient polymer tandem solar cells, the Yang's group has realized NREL certified 10.6% efficient polymer tandem devices.
10. Sargent, E. H. Colloidal Quantum Dot Solar Cells. *Nat. Photon* **2012**, *6*, 133–135.
11. Bernardi, M.; Lohrman, J.; Kumar, P.; Kirkeminde, A.; Ferralis, N.; Grossman, J. C.; Ren, S. Nanocarbon-Based Photovoltaics. *ACS Nano* **2012**, Published online September 6, 2012. DOI: 10.1021/nn302893p.
12. Geim, A. Graphene: Status and Prospects. *Science* **2009**, *323*, 1530–1534.
13. Ci, L.; Song, L.; Jin, C.; Jariwala, D.; Wu, D.; Li, Y.; Srivastava, A.; Wang, Z. F.; Storr, K.; Balicas, L.; *et al*. Atomic Layers of Hybridized Boron Nitride and Graphene Domains. *Nat. Mater.* **2010**, *9*, 430–435.
14. Levendorf, M. P.; Kim, C.-J.; Brown, L.; Huang, P. Y.; Havener, R. W.; Muller, D. A.; Park, J. Graphene and Boron Nitride Lateral Heterostructures for Atomically Thin Circuitry. *Nature* **2012**, *488*, 627–632.
15. Bernardi, M.; Palummo, M.; Grossman, J. C. Optoelectronic Properties in Monolayers of Hybridized Graphene and Hexagonal Boron Nitride. *Phys. Rev. Lett.* **2012**, *108*, 226805.
16. Splendiani, A.; Sun, L.; Zhang, Y.; Li, T.; Kim, J.; Chim, C.-Y.; Galli, G.; Wang, F. Emerging Photoluminescence in Monolayer MoS_2. *Nano Lett.* **2010**, *10*, 1271–1275.
17. Radisavljevic, B.; Radenovic, A.; Brivio, J.; Giacometti, V.; Kis, A. Single-Layer MoS_2 Transistors. *Nat. Nanotechnol.* **2011**, *6*, 147–150.
18. Ataca, C.; Sahin, H.; Ciraci, S. Stable Single-Layer MX2 Transition-Metal Oxides and Dichalcogenides in a Honeycomb-like Structure. *J. Phys. Chem. C* **2012**, *116*, 8983–8999.
19. Nair, R. R.; Blake, P.; Grigorenko, A. N.; Novoselov, K. S.; Booth, T. J.; Stauber, T.; Peres, N. M. R.; Geim, A. K. Fine Structure Constant Defines Visual Transparency of Graphene. *Science* **2008**, *320*, 1308.
20. Miao, X.; Tongay, S.; Petterson, M. K.; Berke, K.; Rinzler, A. G.; Appleton, B. R.; Hebard, A. F. High Efficiency Graphene Solar Cells by Chemical Doping. *Nano Lett.* **2012**, *12*, 2745–2750.
21. Gao, G.; Gao, W.; Cannuccia, E.; Taha-Tijerina, J.; Balicas, L.; Mathkar, A.; Narayanan, T. N.; Liu, Z.; Gupta, B. K.; Peng, J.; *et al*. Artificially Stacked Atomic Layers: Towards New van der Waals Solids. *Nano Lett.* **2012**, 3518–3525.
22. Song, J. C. W.; Rudner, M. S.; Marcus, C. M.; Levitov, L. S. Hot Carrier Transport and Photocurrent Response in Graphene. *Nano Lett.* **2011**, *11*, 4688–4692.
23. Gabor, N. M.; Song, J. C. W.; Ma, Q.; Nair, N. L.; Taychatanapat, T.; Watanabe, K.; Taniguchi, T.; Levitov, L. S.; Herrero, P. J. Hot Carrier-Assisted Intrinsic Photoresponse in Graphene. *Science* **2011**, *334*, 648–652.
24. Lui, C. H.; Mak, K. F.; Shan, J.; Heinz, T. Ultrafast Photoluminescence from Graphene. *Phys. Rev. Lett.* **2010**, *105*, 127404.
25. Franceschetti, A. Nanostructured Materials for Improved Photoconversion. *MRS Bull.* **2011**, *36*, 192–197.
26. Though other geometries for C and BN domains are possible, such as quantum dots of BN in C (or *vice versa*), the results presented here refer to structures lacking confinement in one of the two directions within the monolayer. When confinement is introduced in both directions by forming dots (*e.g.* see Li, J.; Shenoy, V. B. *Appl. Phys. Lett.* **2011**, *98*, 013105), the DFT band gaps are usually higher than those found here.
27. Liu, L.; Feng, Y. P.; Shen, Z. X. Structural and Electronic Properties of *h*-BN. *Phys. Rev. B* **2003**, *68*, 104102.
28. Giannozzi, P.; Baroni, S.; Bonini, N.; Calandra, M.; Car, R.; Cavazzoni, C.; Ceresoli, D.; Chiarotti, G. L.; Cococcioni, M.; Dabo, I.; *et al*. QUANTUM ESPRESSO: a Modular and Open-Source Software Project for Quantum Simulations of Materials. *J. Phys.: Condens. Matter* **2009**, *21*, 395502 (19pp).
29. Kanai, Y.; Grossman, J. C. Role of Semiconducting and Metallic Tubes in P3HT/Carbon-Nanotube Photovoltaic Heterojunctions: Density Functional Theory Calculations. *Nano Lett.* **2008**, *8*, 908–912.
30. Giantomassi, M.; Stankovski, M.; Shaltaf, R.; Gruning, M.; Bruneval, F.; Rinke, P.; Rignanese, G.-M. Electronic Properties of Interfaces and Defects from Many-Body Perturbation Theory: Recent Developments and Applications. *Phys. Status Solidi B* **2011**, *248*, 275–289.
31. Note that in this work ΔE_v is the same at all levels of theory, since the GW corrections found here fall almost entirely on

the LUMO level and were thus applied as a scissor correction, as further explained in Methods.
32. Given the choice of working with superlattices instead of dots geometries, we remark that this is a lower bound of the C domain size for this effect to be observed in practice.
33. Shockley, W.; Queisser, H. J. Detailed Balance Limit of Efficiency of p−n Junction Solar Cells. *J. Appl. Phys.* **1961**, *32*, 510–519.
34. Scharber, M. C.; Muhlbacher, D.; Koppe, M.; Denk, P.; Waldauf, C.; Heeger, A. J.; Brabec, C. J. Design Rules for Donors in Bulk-Heterojunction Solar Cells—Towards 10% Energy-Conversion Efficiency. *Adv. Mater.* **2006**, *18*, 789–794.
35. Lunt, R. R.; Osedach, T. O.; Brown, P. R.; Rowehl, J. A.; Bulovic, V. Practical Roadmap and Limits to Nanostructured Photovoltaics. *Adv. Mater.* **2011**, *23*, 5712–5727.
36. The AM1.5G spectrum was taken from the NREL website: http://rredc.nrel.gov/solar/spectra/am1.5 and integrated with the trapezoid rule.
37. Perez, M. D.; Borek, C.; Forrest, S. R.; Thompson, M. E. Molecular and Morphological Influences on the Open Circuit Voltages of Organic Photovoltaic Devices. *J. Am. Chem. Soc.* **2009**, *131*, 9281–9286.
38. Reference 34 uses 65% for both the FF and the EQE. However, XSC with up to 75% of both the FF and EQE have been shown recently in the literature (ref 35). The alternative choice of using this 75% limit for both FF and EQE would lead to a decrease in the efficiency by a factor $0.65/0.75^2 \approx 1.15$ compared to the values reported here. In addition, we note that different from ref 34, in our work $\Delta E_c > 0$ suffices to guarantee exciton dissociation at the interface, since the optical donor band gap is used instead of the electronic gap.
39. Sutter, P. Growth and Characterization of Graphene−Boron Nitride Heterostructures. March meeting of the American Physical Society of 2012, Boston MA. Abstract available at http://meetings.aps.org/link/BAPS.2012.MAR.X12.5.
40. Miyake, T.; Saito, S. Quasiparticle Band Structure of Carbon Nanotubes. *Phys. Rev. B* **2003**, *68*, 155424.
41. Ross, R. T.; Nozik, A. J. Efficiency of Hot-Carrier Solar Energy Converters. *J. Appl. Phys.* **1982**, *53*, 3813–3818.
42. Cabanillas-Gonzales, J.; Grancini, G.; Lanzani, G. Pump-Probe Spectroscopy in Organic Semiconductors: Monitoring Fundamental Processes of Relevance in Optoelectronics. *Adv. Mater.* **2011**, *23*, 5468–5485.
43. Perdew, J.; Burke, K.; Ernzerhof, M. Generalized Gradient Approximation Made Simple. *Phys. Rev. Lett.* **1996**, *77*, 3865–3868.
44. Vanderbilt, D. Soft Self-Consistent Pseudopotentials in a Generalized Eigenvalue Formalism. *Phys. Rev. B* **1990**, *41*, 7892–7895.
45. Monkhorst, H. J.; Pack, J. D. Special Points for Brillouin-Zone Integrations. *Phys. Rev. B* **1976**, *13*, 5188–5192.
46. Rydberg, H.; Dion, M.; Jacobson, N.; Schroder, E.; Hyldgaard, P.; Simak, S. I.; Langreth, D. C.; Lundqvist, B. I. Van der Waals Density Functional for Layered Structures. *Phys. Rev. Lett.* **2003**, *91*, 126402.
47. Marini, A.; Hogan, C.; Gruning, M.; Varsano, D. Yambo: An *ab Initio* Tool for Excited State Calculation. *Comput. Phys. Commun.* **2009**, *180*, 1392–1403.
48. Perdew, J. P.; Zunger, A. Self-Interaction Correction to Density-Functional Approximations for Many-Electron Systems. *Phys. Rev. B* **1981**, *23*, 5048–5079.
49. Troullier, N.; Martins, J. L. Efficient Pseudopotentials for Plane-Wave Calculations. *Phys. Rev. B* **1991**, *43*, 1993–2006.
50. Akaike, K.; Kanai, K.; Yoshida, H.; Tsutsumi, J.; Nishi, T.; Sato, N.; Ouchi, Y.; Seki, K. Ultraviolet Photoelectron Spectroscopy and Inverse Photoemission Spectroscopy of [6,6]-Phenyl-C_{61}-Butyric Acid Methyl Ester in Gas and Solid Phases. *J. Appl. Phys.* **2008**, *104*, 023710.
51. Blase, X.; Attaccalite, C.; Olevano, V. First-Principles GW Calculations for Fullerenes, Porphyrins, Phtalocyanine, and Other Molecules of Interest for Organic Photovoltaic Applications. *Phys. Rev. B* **2011**, *83*, 115103.
52. Sato, N.; Seki, K.; Inokuchi, H. Polarization Energies of Organic Solids Determined by Ultraviolet Photoelectron Spectroscopy. *J. Chem. Soc.: Faraday Trans. 2* **1981**, *77*, 1621–1633.
53. Lyons, L. E. Photo- and Semi-conductance in Organic Crystals. Part V. Ionized States in Molecular Crystals. *J. Chem. Soc.* **1957**, 5001–5007.